Discrete dislocation plasticity analysis of static friction

Deshpande, VS; Needleman, A; van der Giessen, Erik

Published in:
Acta Materialia

DOI:
10.1016/j.actamat.2004.03.018

Available online at www.sciencedirect.com
SCIENCE DIRECT®
Acta Materialia 52 (2004) 3135–3149
Acta MATERIALIA
www.actamat-journals.com

Discrete dislocation plasticity analysis of static friction

V.S. Deshpande [a], A. Needleman [b,*], E. Van der Giessen [c]

[a] Department of Engineering, Cambridge University, Trumpington Street, Cambridge CB2 1PZ, UK
[b] Division of Engineering, Brown University, 182 Hope Street, Providence, RI 02912, USA
[c] Department of Applied Physics, University of Groningen, Nyenborgh 4, 9747 AG Groningen, The Netherlands

Received 6 February 2004; received in revised form 10 March 2004; accepted 12 March 2004
Available online 26 April 2004

Abstract

The initiation of frictional sliding between a flat-bottomed indenter and a planar single-crystal substrate is analyzed using discrete dislocation dynamics. Plastic deformation is modeled through the motion of edge dislocations in an elastic solid with the lattice resistance to dislocation motion, dislocation nucleation, dislocation interaction with obstacles and dislocation annihilation incorporated through a set of constitutive rules. The adhesion between the indenter and the substrate is modeled using a shear traction versus sliding displacement cohesive relation. Two cohesive relations are used. In both relations, the shear traction increases to a maximum value, subsequently in one relation the shear traction decays to zero with increasing sliding, while in the other relation the shear traction remains at its maximum value. Predictions obtained using these two cohesive relations do not differ qualitatively and the quantitative differences are small. The shear stress needed to initiate sliding is a function of contact size; for large contacts sliding initiates at a value approximately equal to the tensile yield strength while for small contacts sliding initiates at the cohesive strength. The effects of superposed normal pressure on the contact, of cohesive strength and of dislocation source density are investigated.

Keywords: Dislocations; Mechanical properties; Friction; Plastic; Size effects; Computer simulation

1. Introduction

The physical mechanisms responsible for the frictional resistance to sliding of unlubricated solid surfaces was established by the work of Bowden and Tabor [1]. The inevitable roughness of practical surfaces results in the real area of intimate contact being generally only a small fraction of the apparent area of contact. Bowden and Tabor [1] proposed that the areas of intimate contact would adhere (cold weld) and that the resistance to sliding (friction force) could be separated into two parts: the "adhesion" term exerted at the interface of real contact and the "ploughing" term arising from inelastic deformation of the surface asperities.

Frictional sliding is a complex process involving multi-asperity contact, large plastic strains and strain gradients, giving rise to high dislocation densities and complex dislocation structures, see for example [2,3]. As a consequence, modeling efforts have tended to focus on specific aspects of this complex process. Asperity contact has been extensively analyzed using conventional plasticity theory including single-asperity contact as well as the elastic–plastic deformation of interacting asperities, e.g., [4–10]. Polonsky and Keer [11,12] used discrete dislocation dynamics to model elastic–plastic deformation of micro-contacts on scales too small to apply conventional continuum plasticity theory. Their analysis revealed that when the asperity size becomes comparable to the dislocation source spacing, the asperities can sustain considerably higher loads than those predicted by continuum plasticity. However, even with these enhanced ploughing forces the model under-predicted the experimentally observed frictional forces. This result is consistent with the original experiments of Bowden and Tabor [1] which showed that the adhesion term can dominate the frictional resistance.

* Corresponding author. Tel.: +1-401-863-2863; fax: +1-401-863-9009.
E-mail address: needle@engine.brown.edu (A. Needleman).

1359-6454/$30.00
doi:10.1016/j.actamat.2004.03.018

Bowden and Tabor [1] developed a theory of a "plastic junction" in which it is postulated that the friction force F_{fr} necessary to slide across a single-asperity is proportional to the area of the contact A_c via

$$F_{fr} = \tau_{fr} A_c, \tag{1}$$

implying that the friction stress τ_{fr} is independent of the contact area. Typical values of A_c for dry adhesive contact in the atomic force microscope are in the range 30–60 nm^2 whereas in the surface force apparatus, A_c is usually in the range 5×10^9–2×10^{11} nm^2. Recent advances in experimental techniques, in particular the development of the atomic force microscope (AFM) and the surface force apparatus (SFA) have made it possible to measure τ_{fr} at nanometer and micrometer levels, although there are at present only a few such measurements. Homola et al. [13] investigated the contact between two mica surfaces using the SFA and obtained $\tau_{fr} \approx 20$ MPa or $\tau_{fr}/\mu \approx 1/1300$, where μ is the shear modulus of mica. On the other hand, for contact between a flat mica surface and a platinum AFM tip, Carpick et al. [14,15] observed that $\tau_{fr} \approx 900$ MPa or $\tau_{fr}/\mu \approx 1/40$, where μ in this case is an "effective" shear modulus for the interface between the two materials. Thus, in terms of the effective shear modulus, τ_{fr} is about 30 times larger in the AFM experiments than the value measured in the SFA. Since the contact area in the AFM is much smaller than that in the SFA, this suggests that τ_{fr} decreases as the size of the contact increases, in contradiction to the original hypothesis of Bowden and Tabor [1].

Hurtado and Kim [16,17] analyzed these scale effects using a discrete dislocation model and demonstrated that there exist three regimes in the variation of τ_{fr} with contact size. For relatively large contacts, τ_{fr} is equal to the Peierls stress while for very small contacts τ_{fr} is equal to the theoretical shear strength of the solid. The transition between these two regimes is governed by the stress to nucleate a dislocation loop at the edge of the contact. For a contact radius a, the Rice and Thompson [18] model predicts that $\tau_{fr} \propto a^{-1/2}$ in this intermediate regime. Hurtado and Kim [16,17] modeled mica contacts and assumed that no dislocation activity occurs in the bulk, with slip solely due to dislocations along the interface.

Bhushan and Nosonovsky [19] arrived at a scaling based on strain-gradient plasticity to model size effects in metal contacts. Arguing that the size of the interface zone over which plasticity occurs scales with the contact size, Bhushan and Nosonovsky [19] obtained a scaling for τ_{fr} similar to that in Hurtado and Kim [16,17]. Molecular dynamics simulations of friction have also been carried out, e.g. Landman et al. [20], Gerde and Marder [21], but the size (and time) scales that can currently be analyzed with molecular dynamics precludes consideration of the full range of scales over which the size effects in friction occur.

Here, we analyze the initiation of sliding between a flat-bottomed indenter and a planar metallic single-crystal substrate. The adhesion between the indenter and the substrate is modeled using a cohesive traction versus displacement relation while plasticity in the substrate is modeled via a discrete dislocation plasticity framework. The latter has been used in previous studies to analyze, for example, the bending [22] and fatigue [23] of single crystals. Since the material model is independent of the adhesion model, the plastic and adhesive properties can be varied independently. Our main focus is on the size dependence of the friction stress τ_{fr}.

2. Discrete dislocation formulation

A plane strain analysis of the initiation of sliding between a perfectly flat indenter and a planar single-crystal substrate is carried out. The boundary value problem analyzed is sketched in Fig. 1(a). Plasticity in the substrate is described by the collective motion of discrete dislocations, while the contact between the indenter and the substrate is modeled using a cohesive shear traction versus sliding displacement relation.

The dislocations are treated as line singularities in an isotropic elastic solid with Young's modulus E and Poisson's ratio ν. Adopting Cartesian tensor notation, with geometry changes neglected, the principle of virtual work takes the form

$$\int_A \sigma_{ij}\delta\epsilon_{ij}\,\mathrm{d}A - \int_{S_{coh}} T_i\delta\Delta_i\,\mathrm{d}S = \int_{S_{ext}} T_i\delta u_i\,\mathrm{d}S, \tag{2}$$

where A is the area of the region analyzed, S_{ext} is the external surface on which tractions are applied and S_{coh} the contact area over which the cohesive tractions operate. With the origin of the Cartesian co-ordinate system at the mid-point of the contact region, the cohesive surface spans $-a/2 \leqslant x_1 \leqslant a/2$ along $x_2 = 0$. Furthermore, σ_{ij} are components of the stress tensor, u_i are the displacement field components, Δ_i are the components of the displacement jump across the cohesive surface, the components of the strain tensor are given by

$$\epsilon_{ij} = \frac{1}{2}\left(u_{i,j} + u_{j,i}\right), \tag{3}$$

where $(\,)_{,i}$ denotes differentiation with respect to x_i, and $T_i = \sigma_{ij}n_j$, with n_j the unit outward normal on S_{ext} or S_{coh}.

For computational efficiency, dislocations are confined to a region near the indenter as sketched in Fig. 1(a) and the computations are terminated before any dislocations reach the boundary of this region, which serves to limit the range of deformations analyzed. The boundary conditions involve: (i) imposing displacements in the x_1 direction to simulate the relative sliding of the two contacting surfaces; (ii) a cohesive

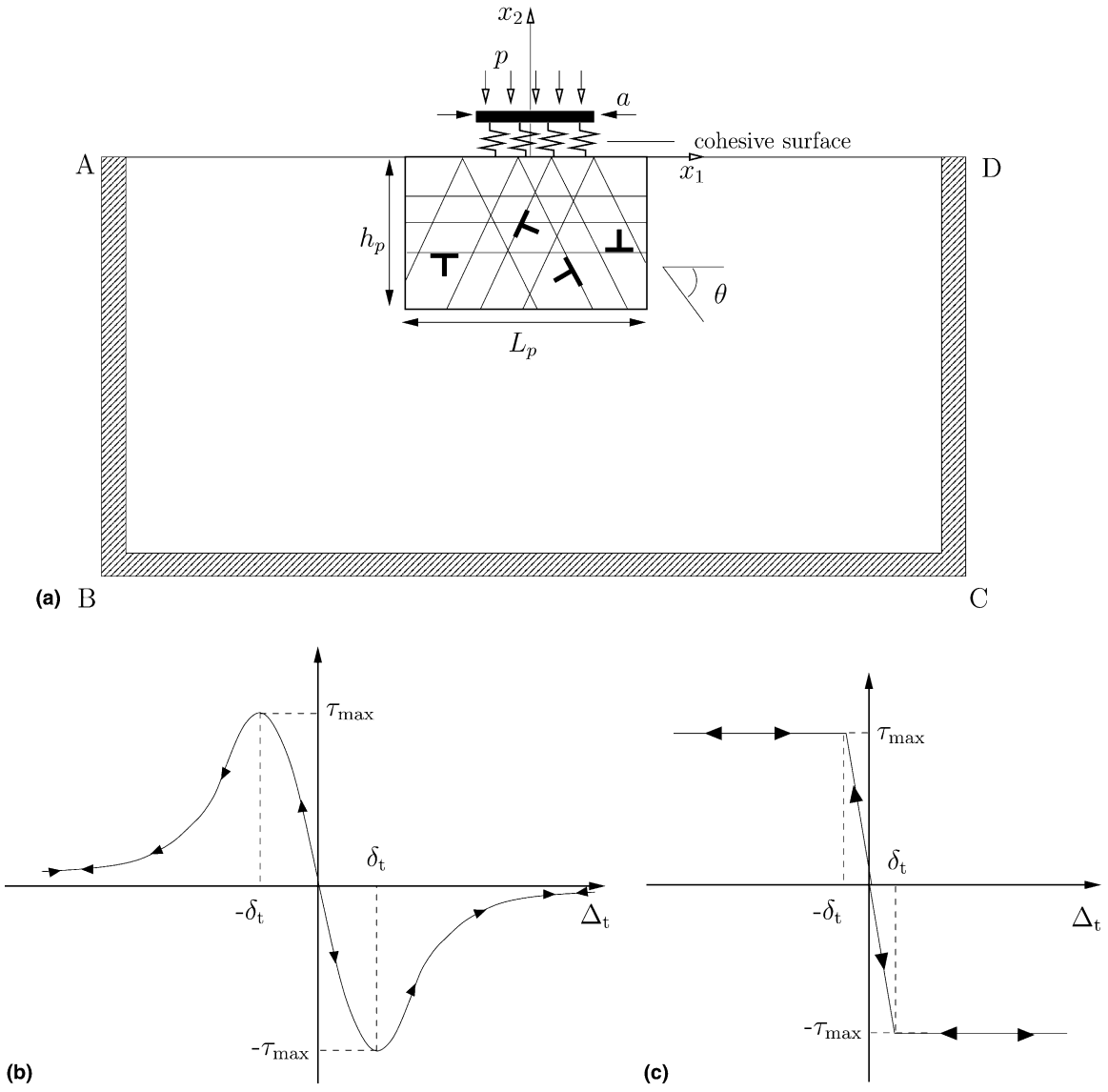

Fig. 1. (a) Sketch of the boundary value problem under consideration; (b) softening cohesive relation and (c) non-softening cohesive relation.

surface that models the adhesion between the two contacting surfaces; and (iii) a normal contact pressure.

Friction being associated with adhesion is an old idea, with Bowden and Tabor [1] using it to develop their concept of a "plastic junction." Numerous researchers have argued that the adhesion arises from the interatomic attractive forces between the two contacting surfaces and hence have employed the Lennard-Jones interaction potential to describe the adhesive interaction; see, for example, [24] for the adhesive interaction between *rigid* spheres and corresponding theories taking into account elastic deformation by Johnson et al. [25] and Derjaguin et al. [26]. More recently, Magius [27], Johnson [28] and Kim et al. [29] have used continuum cohesive formulations to model adhesion in an elastic contact.

There is at present no fundamental basis for choosing the form of cohesive relation to use in conjunction with the discrete dislocation description of material behavior. In our calculations, we neglect any coupling between normal and shear separation in the traction–displacement jump relation and consider the following two limiting cases:

1. A "softening" cohesive relation with a finite cohesive energy, sketched in Fig. 1(b), which is similar to that suggested by Xu and Needleman [30] and used in fracture analyses:

$$T_t = -\sqrt{e}\tau_{max}\frac{\Delta_t}{\delta_t}\exp\left(-\frac{\Delta_t^2}{2\delta_t^2}\right), \tag{4}$$

where $\Delta_t = u_1(x_1, 0)$ is the tangential displacement jump across the cohesive surface, T_t the shear traction and τ_{max} and δ_t are constants. The maximum value of the shear traction $|T_t| = \tau_{max}$ occurs at $|\Delta_t| = \delta_t$ and the shear work of separation $\phi = -\int_0^\infty T_t\,d\Delta_t = \sqrt{e}\tau_{max}\delta_t$.

2. A "non-softening" cohesive relation, sketched in Fig. 1(c), and described by

$$T_{\mathrm{t}} = \begin{cases} -\tau_{\max}\dfrac{\Delta_{\mathrm{t}}}{\delta_{\mathrm{t}}} & \text{if } |\Delta_{\mathrm{t}}| < \delta_{\mathrm{t}}, \\ -\tau_{\max}\mathrm{sign}(\Delta_{\mathrm{t}}) & \text{otherwise.} \end{cases} \tag{5}$$

For this non-softening cohesive relation, the shear work of separation, ϕ, is not finite.

The displacements

$$u_1 = U(t), \tag{6a}$$

$$u_2 = 0, \tag{6b}$$

with $U(t)$ monotonically increasing, are applied on the boundaries AB, BC and CD in Fig. 1(a) to simulate the relative sliding of the contacting surfaces. Since the prescribed material displacement is in the $+x_1$ direction, the indenter is sliding in the $-x_1$ direction relative to the crystal substrate. In addition, when a normal pressure p is prescribed

$$T_2 = -p \quad \text{on} \quad -a/2 \leqslant x_1 \leqslant a/2, \quad x_2 = 0. \tag{7}$$

In most calculations here, the contact pressure, p, is taken to be zero. Regardless of the value of p, the boundary conditions do not restrict the normal displacements along the contact region so that the normal loading is modeled through a 'soft' loading device.

The focus in the calculations is on the initiation of sliding, with our definition of initiation depending on the cohesive relation used; for the softening cohesive relation, Eq. (4), initiation is identified with vanishing shear traction, whereas with the non-softening cohesive relation, Eq. (5), initiation is identified with attaining a specified value of U.

2.1. Method of analysis

The computation of the deformation history is carried out in an incremental manner with the applied loading increased monotonically: when the contact pressure is non-zero, p is first monotonically increased up to the desired value and then the displacements in Eq. (6) applied with the contact pressure fixed. Each time step involves the following computational stages: (i) determining the Peach–Koehler forces on the dislocations; (ii) determining the rate of change of the dislocation structure caused by the motion of the dislocations, generation of new dislocations, annihilation of dislocations, their possible pinning at obstacles and dislocations exiting from the surface $x_2 = 0$; and (iii) determining the stress and strain state for the updated dislocation arrangement.

Following Van der Giessen and Needleman [31], we write the velocity and stress and strain-rate fields as the superposition of two fields given by

$$\dot{u}_i = \dot{\hat{u}}_i + \dot{\tilde{u}}_i, \quad \dot{\epsilon}_{ij} = \dot{\hat{\epsilon}}_{ij} + \dot{\tilde{\epsilon}}_{ij}, \quad \dot{\sigma}_{ij} = \dot{\hat{\sigma}}_{ij} + \dot{\tilde{\sigma}}_{ij}, \tag{8a}$$

where $\dot{(\,)}$ denotes differentiation with respect to time and the $\tilde{(\,)}$ fields are the sum of the fields of the individual dislocations in their current positions, i.e.

$$\dot{\tilde{u}}_i = \sum_{I=1}^{N} \dot{\tilde{u}}_i^{(I)}, \quad \dot{\tilde{\sigma}}_{ij} = \sum_{I=1}^{N} \dot{\tilde{\sigma}}_{ij}^{(I)}, \quad \dot{\tilde{\epsilon}}_{ij} = \sum_{I=1}^{N} \dot{\tilde{\epsilon}}_{ij}^{(I)}. \tag{8b}$$

Here, the individual fields employed are those for an edge dislocation in a half-space, [32], with the traction free surface corresponding to $x_2 = 0$. The $\hat{(\,)}$ fields represent the image fields that correct for the actual boundary conditions and are determined as follows.

At a given time t, the stress field and the current positions of all dislocations are known and the aim is to determine the fields at time $t + \Delta t$. An increment of loading, either an increment in the pressure on the contact surface $\dot{p}\Delta t$ with fixed displacements along the boundaries AB, BC and CD or an increment in the displacements $\dot{U}\Delta t$ along those boundaries with the contact pressure kept fixed, is applied. The rate boundary value problem for the $\hat{(\,)}$ fields is formulated by expanding the virtual work expression Eq. (2) at $t + \Delta t$ to give

$$\int_A \hat{\sigma}_{ij}^{(t+\Delta t)}\delta\epsilon_{ij}\,\mathrm{d}A - \int_{S_{\mathrm{coh}}} T_{\mathrm{t}}^{(t+\Delta t)}\delta\Delta_{\mathrm{t}}\,\mathrm{d}S = -\int_{S_{\mathrm{coh}}} p^{(t+\Delta t)}\delta u_2\,\mathrm{d}S, \tag{9}$$

as the individual dislocations fields $\tilde{\sigma}_{ij}$ satisfy continuing equilibrium together with traction free conditions on $x_2 = 0$. Following Cleveringa et al. [33], the rate form of Eq. (9) is then written as

$$\begin{aligned} &\int_A \dot{\hat{\sigma}}_{ij}\delta\epsilon_{ij}\,\mathrm{d}A + \int_{S_{\mathrm{coh}}} K_{\mathrm{t}}\left(\tilde{\Delta}_{\mathrm{t}}^{(t+\Delta t)} + \hat{\Delta}_{\mathrm{t}}^{(t)}\right)\dot{\hat{\Delta}}_{\mathrm{t}}\delta\Delta_{\mathrm{t}}\,\mathrm{d}S \\ &\quad = -\frac{1}{\Delta t}\left[\int_A \hat{\sigma}_{ij}^{(t)}\delta\epsilon_{ij}\,\mathrm{d}A + \int_{S_{\mathrm{coh}}} p^{(t+\Delta t)}\delta u_2\,\mathrm{d}S \right. \\ &\qquad \left. - \int_{S_{\mathrm{coh}}} T_{\mathrm{t}}\left(\tilde{\Delta}_{\mathrm{t}}^{(t+\Delta t)} + \hat{\Delta}_{\mathrm{t}}^{(t)}\right)\delta\Delta_{\mathrm{t}}\,\mathrm{d}S\right], \end{aligned} \tag{10a}$$

where

$$K_{\mathrm{t}} = -\frac{\partial T_{\mathrm{t}}}{\partial \Delta_{\mathrm{t}}}. \tag{10b}$$

Since the $\hat{(\,)}$ fields are smooth in the region of interest, the rate boundary value problem Eq. (10) is conveniently solved using the finite element method with the displacement boundary conditions along AB, BC and CD in Fig. 1(a)

$$\dot{\hat{u}}_i = \dot{u}_i - \dot{\tilde{u}}_i, \tag{11}$$

inferred from Eq. (6). While solving Eq. (10) suffices in most cases to obtain an equilibrium $\hat{(\,)}$ solution, the linearized rate boundary value problem Eq. (10) requires extremely small time steps ($\Delta t < 0.01$ ns) when dislocations exit the substrate via the cohesive surface. A dislocation leaves a surface step which affects the cohesive traction when exiting the substrate through the cohesive

surface. In the current implementation, an iterative procedure was employed to ensure that the virtual work expression Eq. (9) is satisfied at every time increment. With iteration $m = 0$ referring to the solution of Eq. (10), in iteration $m > 0$ we solve

$$\int_A {}^{(m)}\hat{\sigma}_{ij}\delta\epsilon_{ij}\,\mathrm{d}A + \int_{S_{\mathrm{coh}}} K_{\mathrm{t}}\left(\tilde{\Delta}_{\mathrm{t}}^{(t+\Delta t)} + \hat{\Delta}_{\mathrm{t}}^{(t)} + \sum_{k=0}^{m-1} {}^{(k)}\hat{\Delta}_{\mathrm{t}}\right) {}^{(m)}\hat{\Delta}_{\mathrm{t}}\delta\Delta_{\mathrm{t}}\,\mathrm{d}S$$
$$= -\int_A \left(\hat{\sigma}_{ij}^{(t)} + \sum_{k=0}^{m-1} {}^{(k)}\hat{\sigma}_{ij}\right)\delta\epsilon_{ij}\,\mathrm{d}A - \int_{S_{\mathrm{coh}}} p^{(t+\Delta t)}\delta u_2\,\mathrm{d}S$$
$$+ \int_{S_{\mathrm{coh}}} T_{\mathrm{t}}\left(\tilde{\Delta}_{\mathrm{t}}^{(t+\Delta t)} + \hat{\Delta}_{\mathrm{t}}^{(t)} + \sum_{k=0}^{m-1} {}^{(k)}\hat{\Delta}_{\mathrm{t}}\right)\delta\Delta_{\mathrm{t}}\,\mathrm{d}S, \tag{12}$$

where ${}^{(m)}\hat{\sigma}_{ij}$ and ${}^{(m)}\hat{\Delta}_{\mathrm{t}}$ refer to the increments in $\hat{\sigma}_{ij}$ and $\hat{\Delta}_{\mathrm{t}}$ in the mth iteration. The iterations are repeated until

$$\frac{\|{}^{(m)}\hat{u}_i\|}{\left\|\sum_{k=0}^{m} {}^{(k)}\hat{u}_i\right\|} \leqslant \epsilon_{\mathrm{r}}, \tag{13}$$

where ϵ_{r} is a specified tolerance, ${}^{(k)}\hat{u}_i$ is the displacement increment in the kth iteration and $\|\ \|$ denotes the Euclidean norm. In the current calculations, ϵ_{r} was taken as 0.0001, and typically the solution converged in two to three iterations.

The long-range elastic interactions between dislocations are accounted for directly in the boundary value problem solution. Short range interactions enter through a set of constitutive rules of the type suggested by Kubin et al. [34]. Constitutive rules are specified for: (i) dislocation glide; (ii) annihilation; (iii) nucleation; (iv) obstacle pinning.

The glide velocity $V_{\mathrm{gln}}^{(I)}$ along the slip plane of dislocation I is taken to be linearly related to the Peach–Koehler force through the drag relation

$$V_{\mathrm{gln}}^{(I)} = \frac{1}{B} f^{(I)}, \tag{14}$$

where B is the drag coefficient and the Peach–Koehler force $f^{(I)}$ is given by

$$f^{(I)} = \left(\hat{\sigma}_{ij} + \sum_{J\neq I} \tilde{\sigma}_{ij}^{(J)} + \tilde{\Sigma}_{ij}^{(I)}\right) b_j^{(I)} m_i^{(\alpha)}. \tag{15}$$

Here, $\tilde{\sigma}_{ij}^{(J)}$ is the stress field of dislocation J, $\Sigma_{ij}^{(I)}$ are the non-singular (image) components of $\tilde{\sigma}_{ij}^{(I)}$, $b_j^{(I)}$ the Burger's vector of of dislocation I and $m_i^{(\alpha)}$ the unit normal to the slip system α on which dislocation I resides.

Initially, each slip systems is free of mobile dislocations, but dislocation dipoles are nucleated at point sources that mimic Frank-Read sources. Nucleation occurs when the magnitude of the Peach–Koehler force at a source exceeds a critical value $\tau_{\mathrm{nuc}}b$ during a time period t_{nuc}, where b is the magnitude of the Burger's vector. The distance L_{nuc} between the nucleated dislocations of opposite sign is taken to be specified by

$$L_{\mathrm{nuc}} = \frac{E}{4\pi(1-\nu^2)}\frac{b}{\tau_{\mathrm{nuc}}}. \tag{16}$$

This choice of L_{nuc} ensures that the shear stress of one of these newly generated dislocations acting on the other is balanced by the slip system shear stress τ_{nuc}.

Annihilation of two opposite signed dislocations on a slip plane occurs when they are within a material-dependent critical annihilation distance $L_{\mathrm{e}} = 6b$.

Obstacles to dislocation motion are modeled as points associated with a slip plane. Dislocations on the obstacle slip plane get pinned as they try to pass through that point. Pinned dislocations can only pass through an obstacle when their Peach–Koehler force exceeds an obstacle dependent value $\tau_{\mathrm{obs}}b$.

Dislocations can exit the crystal substrate along the surface $x_2 = 0$, including along the contact area. When dislocations exit the substrate, these dislocation do not contribute to the stress field and are thus not included in calculating the sum $\tilde{\sigma}_{ij} = \sum_{I=1}^{N} \tilde{\sigma}_{ij}^{(I)}$. However, a dislocation which has exited does contribute to the displacement field with a step of magnitude $b/2$ across the slip plane.

3. Numerical results

The size of the region analyzed in the calculations presented here is 1000 μm × 500 μm and a finite element mesh comprising 178 × 100 bilinear quadrilateral elements was employed. Dislocation activity was restricted to a region $L_{\mathrm{p}} \times h_{\mathrm{p}} = 30\ \mu\mathrm{m} \times 10\ \mu\mathrm{m}$ in which the finite element mesh was highly refined and comprised 136 × 45 elements; the mesh was always kept uniform in a square region below the contact surface. Also, the element size in that square region was at least four times smaller than $E\delta_{\mathrm{t}}/\tau_{\max}$ to provide resolution of gradients associated with the cohesive surface.

The single-crystal substrate is taken to have three-slip systems: two-slip systems have their slip planes oriented at $\theta = \pm 60°$ with respect to the contact surface $x_2 = 0$ and the third one at $\theta = 0°$, which gives an FCC type orientation. Each slip system comprises equally placed slip planes $100b$ apart in the process window, where $b = 0.25$ nm is the magnitude of the Burger's vector. Initially, these slip planes are assumed to have no mobile dislocations but to have a random distribution of dislocation sources and obstacles.

The value of the drag coefficient is taken to be $B = 10^{-4}$ Pa s, which is a representative value for aluminum [34]. The sources nucleate a dipole when the Peach–Koehler force exceeds a critical value of $\tau_{\mathrm{nuc}}b$ during a period of time $t_{\mathrm{nuc}} = 10$ ns; τ_{nuc} for the sources is taken to have a Gaussian distribution with a mean source strength $\bar{\tau}_{\mathrm{nuc}} = 50$ MPa and a standard deviation of 10 MPa. Thus, from Eq. (16) the mean nucleation

length $L_{\text{nuc}} = 125b$, with $E = 70$ GPa and $\nu = 0.33$, which are representative of aluminum.

Unless otherwise specified, results pertain to the "non-softening" cohesive relation, Eq. (5), with the density of the point sources and obstacles taken to be $\rho_{\text{src}} = 72/\mu\text{m}^2$ and $\rho_{\text{obs}} = 124/\mu\text{m}^2$, respectively. The cohesive properties are taken to be $\tau_{\max} = 300$ MPa and $\delta_t = 0.5$ nm.

Resolving the dislocation dynamics requires a small time step of $\Delta t = 0.5$ ns. To reduce the computing time, the calculations were carried out with rather high loading rates; $\dot{U}/a = 10^4$/s and, when a pressure is prescribed on the contact area, $\dot{p} = 10^5$ GPa/s. The effect of loading rate is not explored but similar to the findings of Cleveringa et al. [35] for crack growth, we expect that here too the high loading rates will not qualitatively change the behavior although the amount of plastic deformation is expected to increase at lower loading rates.

The tensile stress versus strain response for three sets of source and obstacle distributions are shown in Fig. 2. The reference material corresponds to $\rho_{\text{src}} = 72/\mu\text{m}^2$. The calculations were carried out on a tensile bar of length $2L = 16$ μm and width $W = 4$ μm with the three-slip systems making angles ±30° and 90° with the tensile axis and an imposed nominal strain-rate of $\dot{U}/L = 100$/s, see Cleveringa et al. [22] for details of such calculations. The stress versus strain behavior is linear up to a yield strength and then after a transient, the overall behavior is essentially non-hardening; the fluctuations are associated with discrete dislocation activity in the relatively small specimen. The flow strength, denoted by σ_Y, is identified with the stress at $\epsilon = 0.0015$ and is ≈50 MPa for the three sets of material parameters (corresponding to a slip-system resolved shear stress of ≈22 MPa). The tensile stress–strain response is not sensitive to specimen size in this range [36].

3.1. Predictions for the reference material properties

Computed curves of average shear stress over the contact length, τ, versus applied displacement, U, with the reference material properties are shown in Fig. 3(a) for contact sizes in the range $0.04\ \mu\text{m} \leqslant a \leqslant 20\ \mu\text{m}$. The contact shear stress τ is given by

$$\tau = -\frac{1}{a}\int_{S_{\text{coh}}} T_1\,\mathrm{d}x_1 \tag{17a}$$

and

$$U = \int_0^t \dot{U}\,\mathrm{d}t. \tag{17b}$$

The value of τ at the initiation of sliding is denoted by τ_{fr} and is referred to as the friction stress.

For contact sizes $a \geqslant 4$ μm, τ first increases approximately linearly with U and then reaches a plateau, while for contact lengths in the range $0.04\ \mu\text{m} \leqslant a \leqslant 2\ \mu\text{m}$, τ continues to increase with increasing U. For the two smallest contacts considered here, $a = 0.1$ and 0.04 μm, no dislocation activity occurs before the cohesive strength of 300 MPa is attained. The horizontal line at $\tau = 300$ MPa is the response of the $a \leqslant 0.6$ μm contacts after the contact shear stress attains the cohesive strength $\tau_{\max} = 300$ MPa.

In Fig. 3(a), for a sufficiently small contact the initiation of sliding is identified with τ attaining the cohesive strength $\tau_{\max}$, while for a sufficiently large contact τ reaches a nearly constant value and this plateau value is

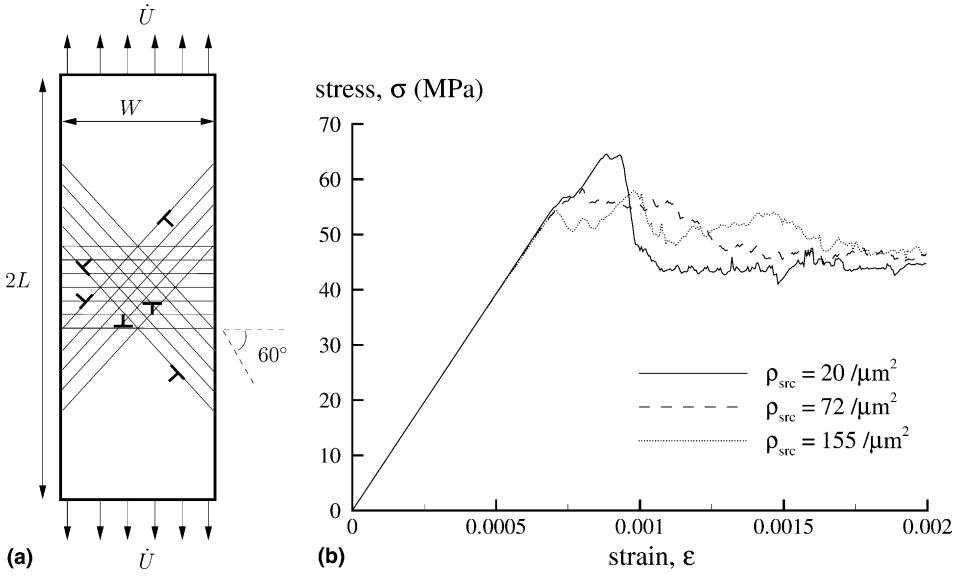

Fig. 2. (a) Sketch of the boundary value problem analyzed to obtain the tensile stress versus strain response of the single crystal, as shown in (b) for three sets of source and obstacle distributions.

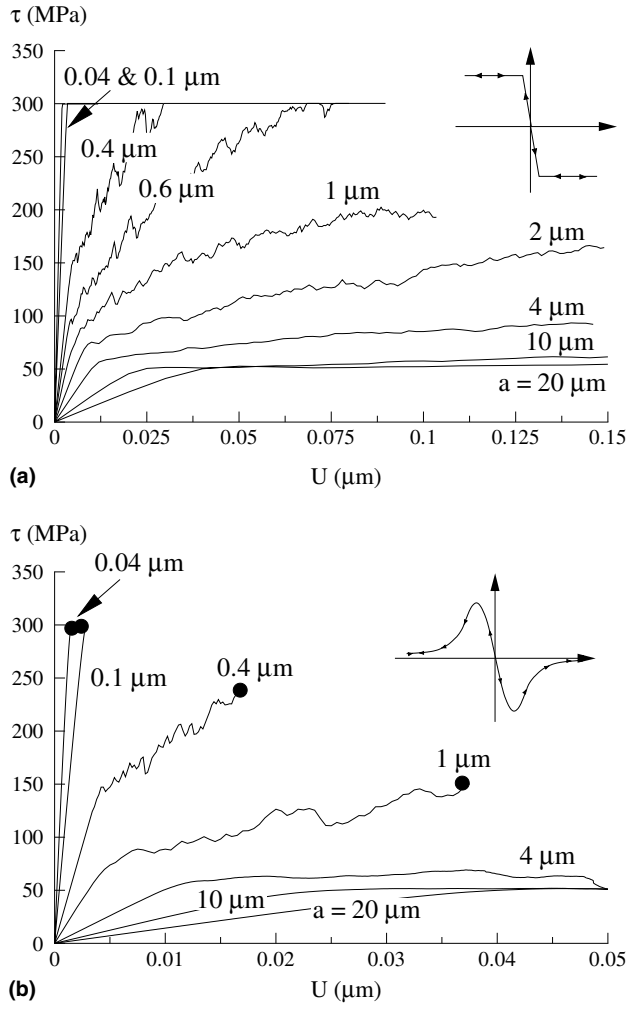

Fig. 3. Friction stress versus displacement response for: (a) non-softening cohesive law (b) softening cohesive relation, for selected values of the contact size a. The filled circles in (b) indicate the value of τ just before it abruptly drops to zero. Sketches of the cohesive relations are shown as insets with each set of curves.

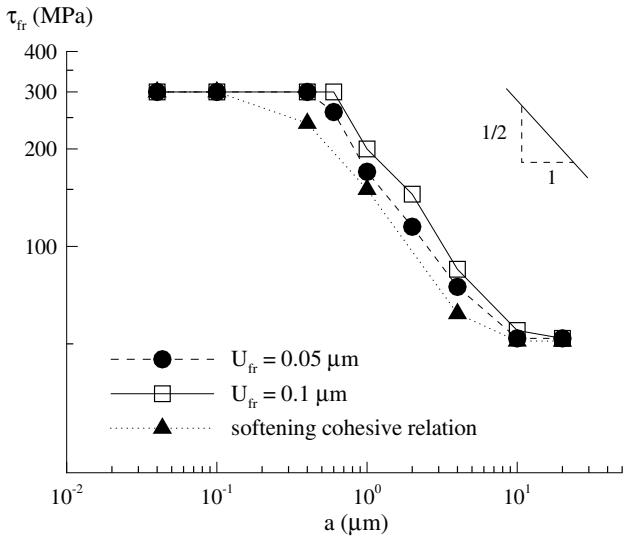

Fig. 4. Friction stress as a function of the contact size. The stresses for two choices of the displacement U_{fr} are shown for the non-softening cohesive relation while τ_{fr} is defined as either the plateau or the value of τ just before the abrupt drop to zero for the softening cohesive relation.

identified with τ_{fr}. In the intermediate regime, for the non-softening cohesive relation, the identification of the value of τ_{fr} is somewhat arbitrary. Here, we identify the initiation of sliding with attaining a specified value of U, denoted by U_{fr}, and τ_{fr} is the value of τ at U_{fr}.

The effect of the contact size a on τ_{fr} using two values of U_{fr}, 0.05 and 0.1 μm, is shown in Fig. 4. For both values of U_{fr}, the τ_{fr} versus a curve exhibits two plateaus: for large contacts ($a \geqslant 10$ μm), τ_{fr} is approximately independent of a with τ_{fr} approximately equal to the tensile flow strength (≈50 MPa), while for small contacts ($a < 0.5$ μm), τ_{fr} is equal to the cohesive strength, $\tau_{fr} = \tau_{max}$. In the transition regime, τ_{fr} is approximately proportional to $a^{-1/2}$. The dependence of τ_{fr} on the choice of U_{fr} is weak, at least for the two values used here.

The number of dislocations per unit contact length N/a, is plotted in Fig. 5(a) as a function of U for the calculations of Fig. 3(a). The value of N/a increases with U for all contacts for which $a > 0.4$ μm. With $a = 0.4$ μm, the contact stress is limited by the cohesive strength and N/a remains constant for $U > 0.03$ μm. In fact, for $a < 0.4$ μm no dislocations are nucleated before τ_{fr} reaches the cohesive strength. The variation of N/a with a (at $U = 0.05$ μm) is shown in Fig. 5(b). The value of N/a is maximum at $a \approx 0.6$ μm and then decreases with no dislocations nucleated for the $a = 0.1$ and 0.04 μm contacts. Contacts with $a \leqslant 0.1$ μm are dislocation source limited elastic contacts for which the friction stress is controlled by the cohesive strength.

The dislocation distributions at $U = 0.05$ μm around the $a = 10$, 2 and 1 μm contacts are shown in Figs. 6(a), (b) and (c), respectively. These figures show that slip on all three-slip systems has been activated, with the $\theta = 0°$ slip system more active near the contact surface. Furthermore, the dislocation density is lower for the $a = 10$ μm contact than for the $a = 2$ and 1 μm contacts, with the majority of the dislocation activity extending approximately 2 μm below the contact surface for $a = 10$ μm and only about 1 μm below the contact surface for the two smaller cases. The higher dislocation density for smaller contacts results in more localized deformation as seen from the deformed meshes (at $U = 0.05$ μm) shown in Figs. 7(a) and (b), for the $a = 10$ and 1 μm contacts, respectively. These deformed mesh plots also show that material is being transported from the rear of the contact (the positive x_1-direction) to the front of the contact (the negative x_1-direction) which results in material piling-up in front of the contact region (recall that the boundary conditions are such that the indenter is sliding in the negative x_1-direction relative

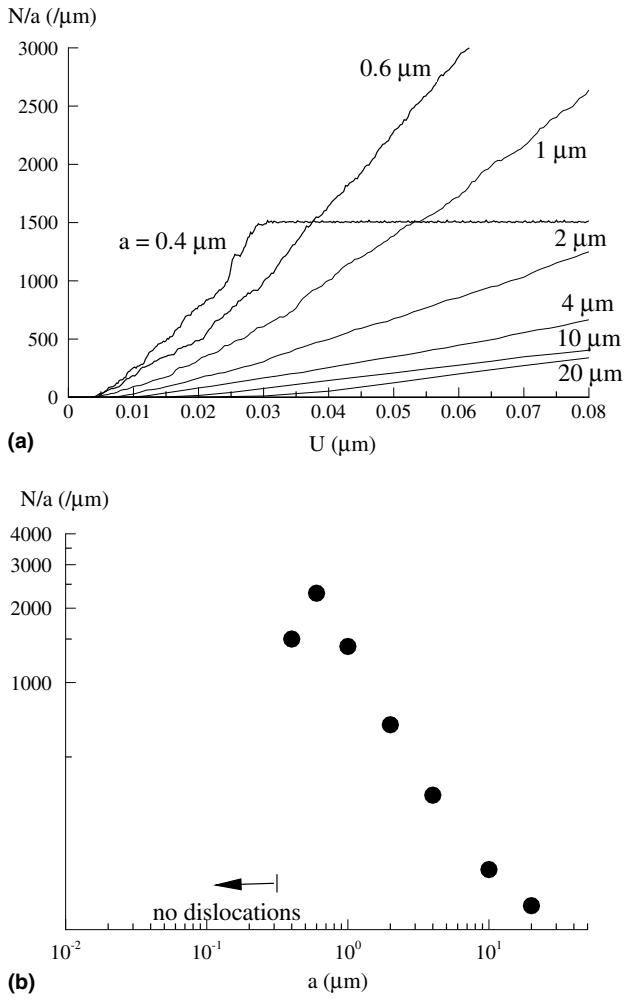

Fig. 5. (a) Number of dislocations N per unit length of the contact as a function of the displacement U. (b) N/a at $U = 0.05$ μm as a function of the contact size a.

to the substrate). The height of the pile-up is larger for the smaller $a = 1$ μm contact. Since the calculations are carried out in an infinitesimal deformation framework, geometry changes are neglected and any effect of ploughing is not accounted for.

Distributions of shear stress, σ_{12}, at $U = 0.05$ μm are shown in Figs. 8(a) and (b) for the $a = 10$ and 1 μm contacts, respectively. While high shear stresses are mainly seen near the edge of the 10 μm contact, the shear stresses are high over the entire contact surface of the 1 μm contact. In addition, bands of highly stressed material emanate at +60° and −60° from the front and rear edges, respectively of the 1 μm contact. These bands are associated with the dislocation pile-ups seen in Fig. 6(c).

3.2. Effect of a softening cohesive relation

Here, we explore the effect of a softening cohesive relation by employing Eq. (4) with $\tau_{max} = 300$ MPa and $\delta_t = 0.5$ nm, i.e. values of the cohesive strength and the shear separation to attain τ_{max} equal to that in the reference case.

The contact stress τ versus sliding displacement U response is plotted in Fig. 3(b) for contact sizes in the range $0.04\ \mu m \leqslant a \leqslant 20\ \mu m$. As in Fig. 3(a), the contact shear stress τ reaches the cohesive strength τ_{max} for small contact sizes and attains a plateau for large contact sizes ($a \geqslant 4$ μm). For intermediate contact sizes, the value of τ in Fig. 3(b) drops to zero rather abruptly at the points marked by filled circles (for clarity the drop is not shown in Fig. 3(b)). Separation with no dislocation activity occurs for sufficiently small contacts ($a \leqslant 0.1$ μm in the calculations here) while considerable dislocation activity precedes fracture for the intermediate contact sizes, $a = 1$ and 0.4 μm.

The predictions of the softening cohesive relation for the variation of the friction stress τ_{fr} with contact size a are included in Fig. 4. Comparison of the softening and non-softening cohesive relation results in Fig. 4 reveals that, while the lower and upper plateaus in the τ_{fr}–a curve remain unaffected, the values of τ_{fr} obtained using the softening cohesive relation are slightly lower than those obtained by employing the non-softening relation for intermediate contact sizes. However, the qualitative features of the τ_{fr}–a curve remain unchanged and the friction stress is still approximately proportional to $a^{-1/2}$ for the intermediate size contacts.

3.3. Effect of source density

The transition from a friction stress approximately equal to the tensile flow strength for large contacts to a friction stress equal to the cohesive strength for small contacts is expected to be affected by the availability of dislocation sources. No dislocations are generated for contacts smaller than 0.4 μm even though the friction stress $\tau_{fr} = \tau_{max} \gg \tau_{nuc}$ – this is a case of source limited behavior. In this section, we investigate the effect of dislocation source density on the predicted friction stress.

Two materials with source and obstacle densities: (i) $\rho_{src} = 20/\mu m^2$, $\rho_{obs} = 35/\mu m^2$ and (ii) $\rho_{src} = 155/\mu m^2$, $\rho_{obs} = 267/\mu m^2$ are considered in addition to the reference material ($\rho_{src} = 72/\mu m^2$ and $\rho_{obs} = 124/\mu m^2$). The tensile stress–strain responses of these two materials are included in Fig. 2. The tensile stress–strain responses of the three materials are similar, with the tensile flow strength ≈50 MPa in all cases.

The variation of the friction stress τ_{fr} (using $U_{fr} = 0.05$ μm) with contact size a is plotted in Fig. 9(a) for all three sets of material parameters. The friction stress τ_{fr} of the $\rho_{src} = 20/\mu m^2$ material is slightly higher than that of the reference material for intermediate size contacts but, as for the reference material, $\tau_{fr} \propto a^{-1/2}$ in that regime. The results for the high dislocation source material, $\rho_{src} = 155/\mu m^2$, differ in that: (i) the friction

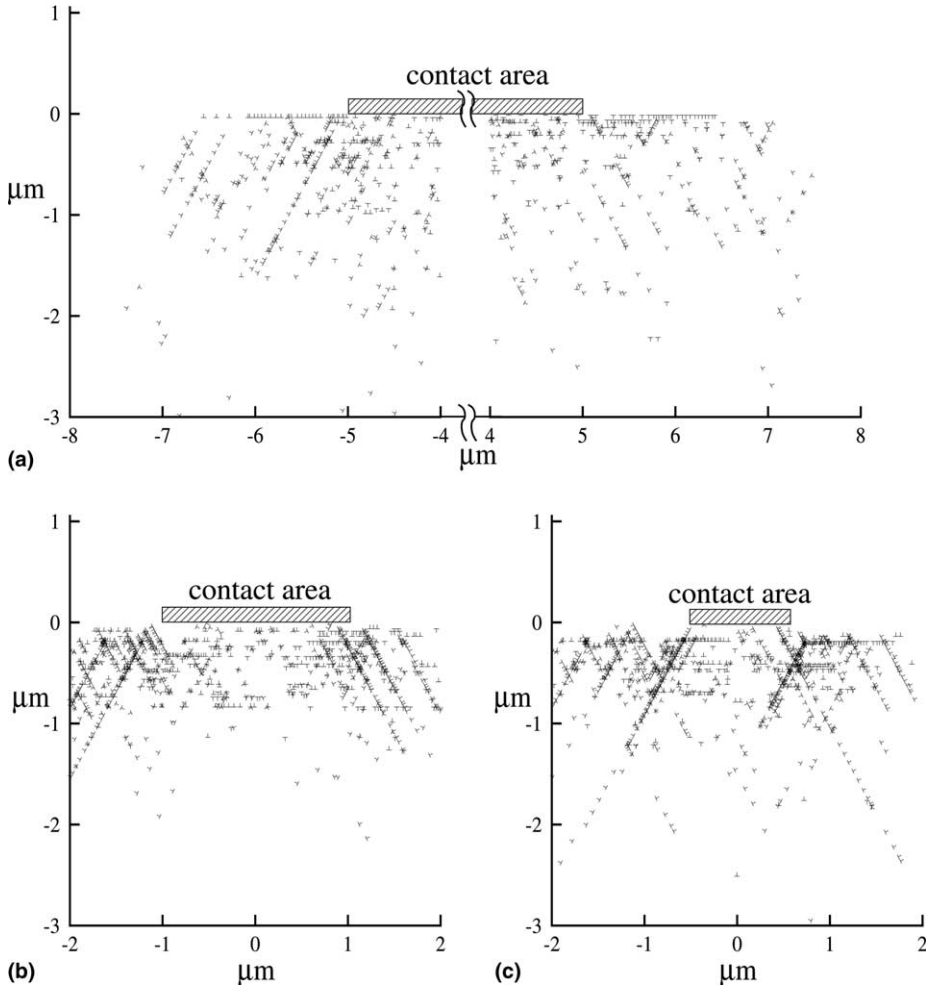

Fig. 6. Dislocation structure at $U = 0.05$ μm for the cases with: (a) $a = 10$ μm, (b) $a = 2$ μm and (c) $a = 1$ μm. The contact surface is indicated in each case.

stress is not proportional to $a^{-1/2}$ for intermediate size contacts and (ii) the upper plateau in the τ_{fr} versus a curve is attained for contacts $a < 0.2$ μm compared to $a < 0.4$ μm for the other two values of ρ_{src}.

Fig. 9(b) shows curves of dislocation density N/a at $U = 0.05$ μm versus a for the three materials. Qualitatively, the dislocation density variation is similar for $\rho_{src} = 20$ and $72/\mu m^2$, with the dislocation density first increasing with decreasing contact size and then reducing to zero for contact sizes $a < 0.4$ μm. However, with $\rho_{src} = 20/\mu m^2$, the dislocation density is about a factor of three smaller than that of the reference material for all contact sizes considered. On the other hand, the dislocation density with $\rho_{src} = 155/\mu m^2$ is greater than that of the reference material for large contacts but lower for intermediate and small contact sizes.

To gain some insight into behavior of the $\rho_{src} = 155/\mu m^2$ material, the dislocation distributions at $U = 0.05$ μm are plotted in Figs. 10(a), (b) and (c), for the $a = 10$, 2 and 1 μm contacts, respectively. A comparison between the corresponding plots in Fig. 6 for the reference material case shows:

(i) The dislocation distributions for the $a = 10$ μm contact are similar for $\rho_{src} = 72/\mu m^2$ (reference value) and for $\rho_{src} = 155/\mu m^2$, but with the dislocation density being higher with $\rho_{src} = 155/\mu m^2$.
(ii) Dislocation activity in the $\rho_{src} = 155/\mu m^2$ material is concentrated much nearer the contact surface for $a = 2$ and 1 μm compared with the corresponding contact sizes in the reference material.

The differences in the deformation mode between the reference ($\rho_{src} = 72/\mu m^2$) and $\rho_{src} = 155/\mu m^2$ materials for the $a = 2$ μm contact is illustrated by plotting contours of slip in Fig. 11. Since dislocation glide gives rise to a displacement jump across the slip plane, the displacement field is not continuous. However, to visualize the deformations, the values of the displacements u_i are evaluated on the finite element mesh with the strain field ϵ_{ij} then obtained by numerical differentiation. Slip $\gamma^{(\alpha)}$ is then defined by

$$\gamma^{(\alpha)} = s_i^{(\alpha)} \epsilon_{ij} m_j^{(\alpha)}, \tag{18}$$

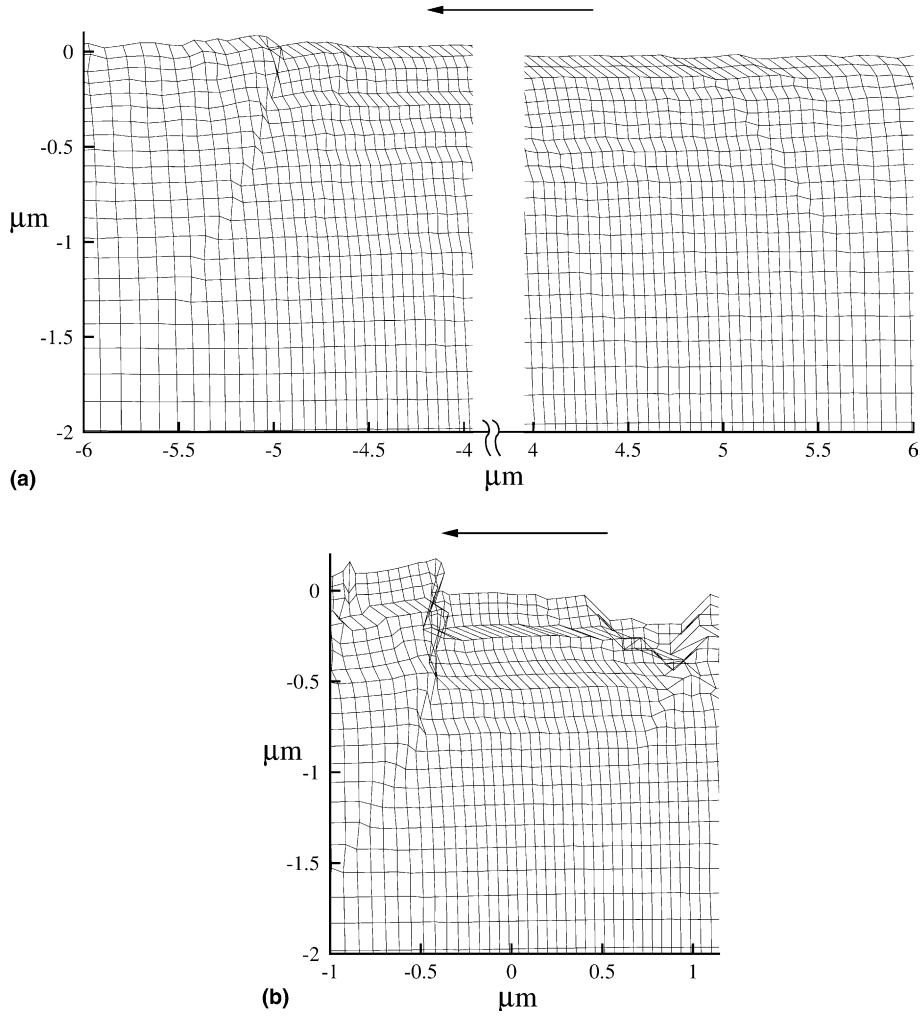

Fig. 7. Deformed mesh at $U = 0.05$ μm for the cases with (a) $a = 10$ μm and (b) $a = 1$ μm. The displacements are magnified by a factor of 10 in both plots. The arrows indicate the direction of sliding of the indenter relative to the substrate.

where $s_i^{(\alpha)}$ is the tangent and $m_j^{(\alpha)}$ is the normal to slip system α. The quantity $\gamma^{(\alpha)}$ is not the actual slip on slip system α as it includes contributions from dislocations gliding on all slip systems; however, it is a convenient quantity for picturing the deformation pattern. Contours of total slip over the three-slip systems, $\Gamma = \sum_{\alpha=1}^{3} |\gamma^{(\alpha)}|$ are plotted in Figs. 11(a) and (b) for the reference and $\rho_{\text{src}} = 155/\mu\text{m}^2$ materials, respectively, at $U = 0.05$ μm. Consistent with the observed differences in the dislocation distributions, large amounts of slip are seen to about 0.5 μm below the contact surface, with some slip occurring to about 1 μm below the contact surface, for the reference material. On the other hand, slip is concentrated at the surface for $\rho_{\text{src}} = 155/\mu\text{m}^2$, with the $\theta = 0°$ slip system most active. It is worth mentioning that the asymptotic non-hardening isotropic continuum plasticity solution predicts that plasticity is concentrated in a vanishingly small band beneath the contact. The present discrete dislocation simulations are consistent with this, provided that there are sufficiently many dislocation sources.

3.4. Effect of normal contact pressure

Conventional models for friction typically assume that the intrinsic friction stress τ_{fr} is independent of the normal contact pressure with the dependence of the macroscopic frictional force on the contact pressure a result of the change in actual contact area, Bowden and Tabor [1]. Here, we present the discrete dislocation plasticity predictions for the effect of contact pressure on the friction stress τ_{fr}.

The variation of the friction stress of the reference material (using the non-softening cohesive relation and $U_{\text{fr}} = 0.05$ μm) with contact area is plotted in Fig. 12 for $p = 100$ and 200 MPa. In these calculations the normal pressure is first increased to the specified level and then the sliding displacement prescribed while keeping the

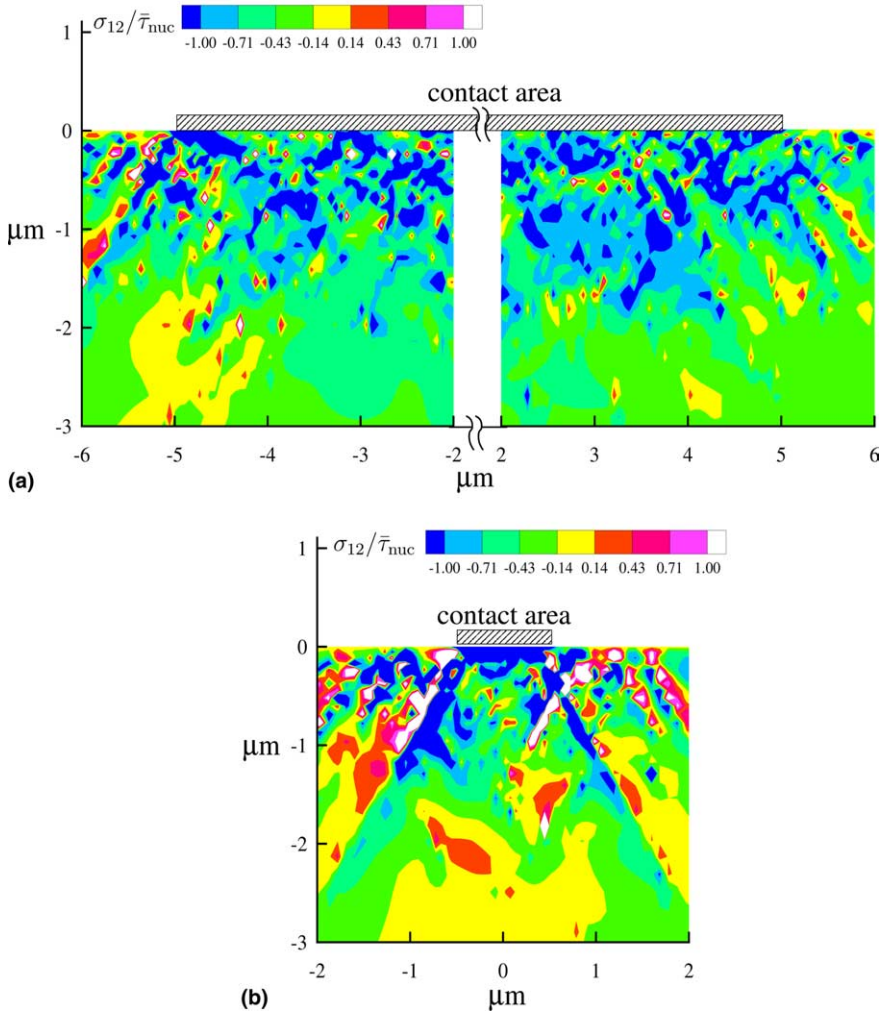

Fig. 8. Contours of the normalized shear stress $\sigma_{12}/\bar{\tau}_{nuc}$ at $U = 0.05$ μm for the cases with (a) $a = 10$ μm and (b) $a = 1$ μm. The contact surface is indicated in each case.

pressure constant. For comparison purposes, the zero contact pressure case from Fig. 4 is also shown. With $p = 100$ MPa, only a small amount of dislocation activity takes place prior to the application of the sliding displacement. Fig. 12 shows that τ_{fr} is largely unaffected by a pressure $p = 100$ MPa. When the contact pressure p is increased to 200 MPa, the value of the friction stress is considerably reduced for larger contacts, where τ_{fr} is governed by plastic flow, but is unaffected for smaller contacts, for which there is negligible dislocation activity.

3.5. Effect of the cohesive strength

A cohesive strength $\tau_{max} = 300$ MPa was employed in all calculations reported in the previous sections. This is much smaller than the inter-atomic bond strength of solids which may govern adhesion at smaller scales. Here, we explore the effect of varying the cohesive strength on the discrete dislocation predictions of the size dependence of the friction stress.

Calculations for $\tau_{max} = 600$ and 150 MPa were carried out with τ_{max}/δ_t still equal to the reference value of 600 MPa/nm and all other reference material properties unchanged. The friction stress τ_{fr} (using $U_{fr} = 0.05$ μm) is plotted in Fig. 13 as a function of the contact size a. The friction stress is seen to be negligibly affected by the cohesive strength for the larger contacts confirming that the lower plateau of the τ_{fr} versus a curve is governed by the plastic properties of the substrate. However, the size of the transition region from the lower to the upper plateau increases with increasing cohesive strength: the transition to the upper plateau occurs at $a \approx 1$ μm for $\tau_{max} = 150$ MPa compared to $a \approx 0.2$ μm for $\tau_{max} = 600$ MPa. Intriguingly, τ_{fr} in the transition region between the two plateaus is relatively unaffected by the cohesive strength. This suggests that the size effects in this region are mainly due to substrate plasticity.

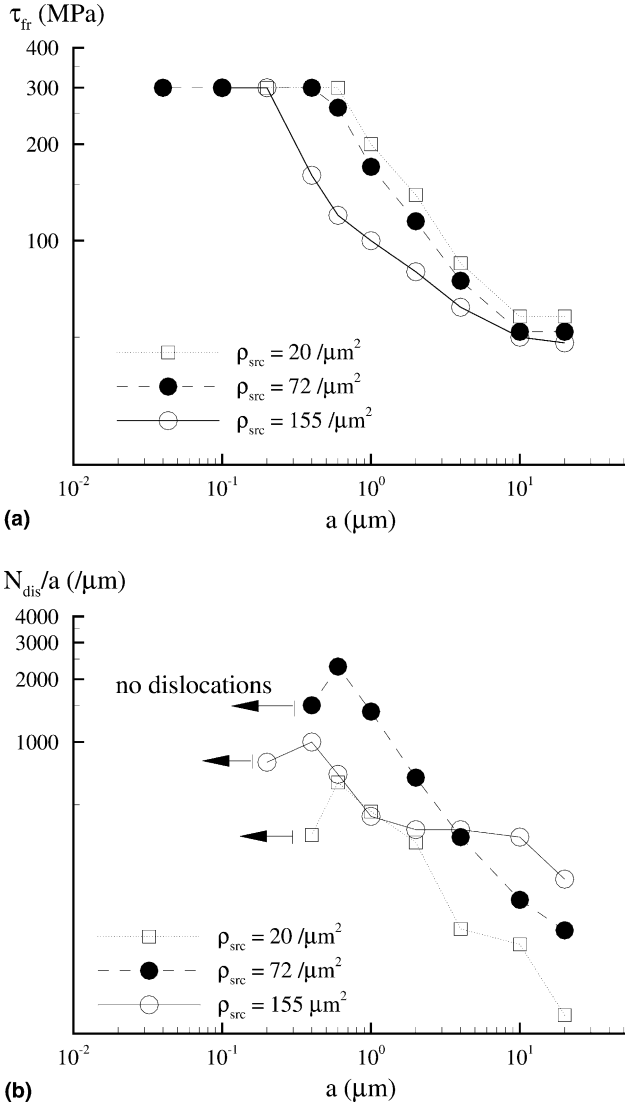

Fig. 9. (a) Effect of source (and obstacle) density on the friction stress and (b) the corresponding number of dislocations per unit contact length. In both cases, the results are plotted at $U = 0.05$ μm. The non-softening cohesive law is used and the results for the reference material with $\rho_{src} = 72/\mu m^2$ are the same as those shown in Figs. 4 and 5(b).

4. Discussion

We have carried out discrete dislocation plasticity analyses of the initiation of sliding between a flat-bottomed indenter and a planar single-crystal substrate. For a sufficiently small contact area, the contact shear stress τ, defined in Eq. (17a), increases linearly with sliding displacement, U, until the cohesive strength is attained. On the other hand, for a sufficiently large contact area, the contact shear stress reaches a plateau at about the tensile yield strength. In both these limiting cases, the friction stress, τ_{fr}, is independent of the nature of the post-peak cohesive relation. When the contact size is between these two limiting cases, the assumed form of the cohesive relation does come into play. For the softening cohesive relation, τ_{fr} is identified with the maximum value of τ prior to the initiation of decohesion, while for the non-softening cohesive relation the identification of τ_{fr} is somewhat arbitrary and we have identified τ_{fr} as the value of τ at a specified sliding displacement U_{fr}. At least for the values of U_{fr} considered, the friction stress is not sensitive to the precise value of U_{fr} or to the choice made for the post-peak cohesive response. Our results are consistent with the observations of Carpick et al. [14,15] and Homola et al. [13] in predicting a substantially higher sliding resistance at the AFM scale than at the SFA scale. However, at present experimental data is not available on the form of the size dependence in the transition regime.

For "sufficiently small" contact sizes, plasticity is source limited and plays no role with the friction stress set by the cohesive properties. However, what "sufficiently small" is depends on the dislocation source density (Fig. 9) and on the cohesive strength (Fig. 13). At higher source densities (and therefore smaller source spacings), plasticity comes into play at smaller contact sizes. The main role of the cohesive strength is to determine when plasticity comes into play: the friction stress, τ_{fr}, versus contact size, a, curve is essentially independent of the cohesive strength between the two τ_{fr} plateaus (Fig. 13). If the cohesive strength is identified with the theoretical shear strength, and assuming that a representative value of the theoretical shear strength is 1/20 the elastic shear modulus, which is about 1.3 GPa for the elastic constants used in the calculations here, an extrapolation of the curves in Fig. 13 gives a transition contact size of $\approx$50 nm for this cohesive strength.

The circumstances modeled in our analyses are quite different from those modeled by Hurtado and Kim [16,17]; Hurtado and Kim [16,17] considered circumstances where dislocation nucleation only occurred at the edge of the contact whereas in our calculations all dislocations originate from Frank-Read sources initially present in the material. Nevertheless, the results of the two analyses exhibit a number of common features. Hurtado and Kim [16,17] predicted a size dependent friction stress τ_{fr} separated into three regimes: (i) for small contacts, τ_{fr} is size independent and equal to the theoretical shear strength; (ii) for sufficiently large contacts, slip occurs by multiple dislocation-cooperative slip, which is a dislocation mobility controlled process and τ_{fr} is equal to an effective Peierls stress; and (iii) in the transition between these two regimes, the friction stress is governed by the singular field required to nucleate a dislocation at the edge of the contact, which gives rise to an inverse square root size dependence. While our analyses exhibit similar plateaus and a transition region with an inverse square root size dependence (for a certain parameter range), the governing parameters differ. For example, in our calculations the Peierls stress is zero and the lower plateau is governed by the

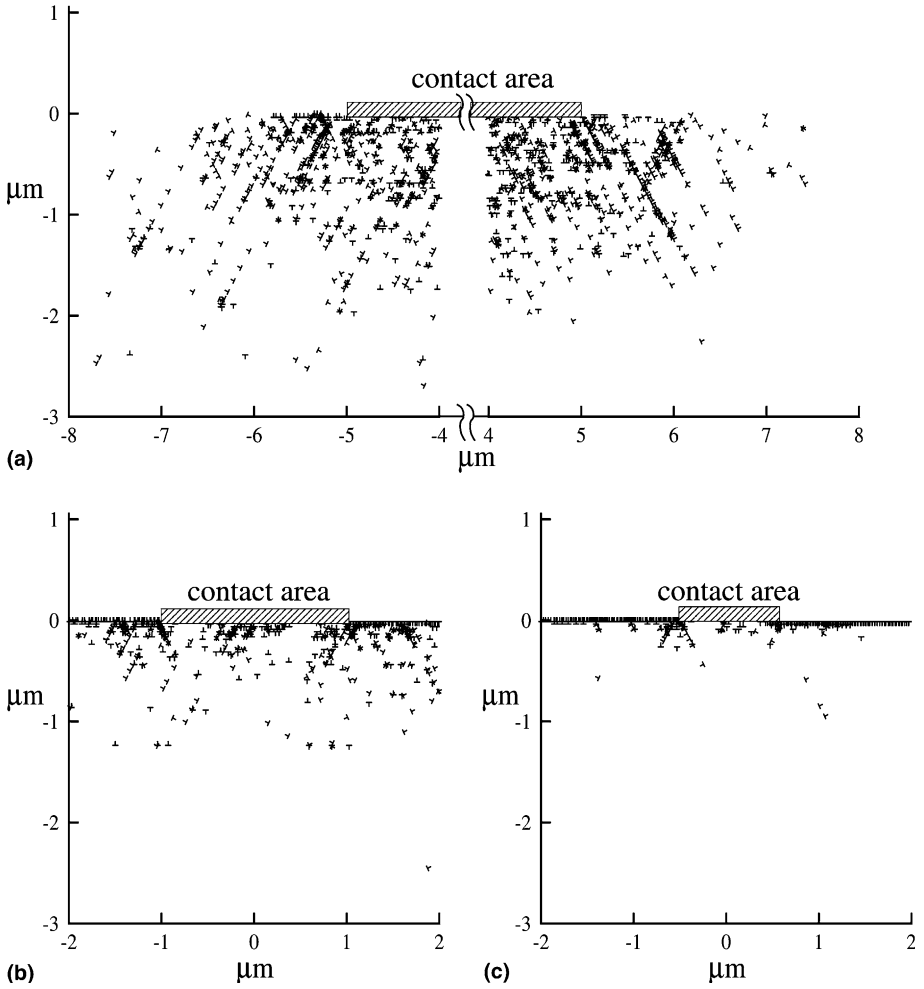

Fig. 10. Dislocation structure at $U = 0.05$ μm for the cases with: (a) $a = 10$ μm, (b) $a = 2$ μm and (c) $a = 1$ μm for the material with $\rho_{src} = 155/\mu m^2$. The contact surface is indicated in each case.

yield strength with dislocation nucleation occurring through internal sources so that the source spacing (or density) is a key parameter and the square root size dependence in the transition regime is lost for a sufficiently large source density. The transition from substrate plasticity governed friction to interface cohesion governed friction is a consequence of source limited plasticity in our analyses. Thus, the value of τ_{fr} is mainly controlled by substrate plasticity with the cohesive strength mainly setting the upper-shelf in the friction stress versus contact size relation.

In molecular dynamics studies of friction, some appropriately chosen interaction potential is taken to connect atoms across the contact surface and provide "surface adhesion." This interaction involves irreversible "snap-throughs" into local energy minima. As noted by Johnson [37], a model of interlocking elastic asperities, such as that proposed by Caroli and Nozieres [38], would also give analogous behavior, albeit at larger length scales. The non-softening cohesive relation employed in the current analysis can represent either of these scenarios. While the unstable interactions and the snap-throughs can be more accurately represented by a periodic shear traction–displacement relation, such as that of Beltz and Rice [39], the non-softening cohesive relation can be viewed as the Maxwell construction to an oscillating shear traction versus displacement relation.

The results here pertain to the initiation of sliding along a perfectly flat surface. Although the analyses are carried out within a framework where geometry changes are neglected, the deformed mesh plots in Fig. 7 show that the mode of plastic deformation is such that an asperity is created in front of the contact region before sliding initiates. Hence, for contact sizes in the regime where significant plastic flow occurs, the continuation of sliding is expected to be affected by asperity ploughing even for an initially very smooth interface. It is also interesting to note that relatively more roughness develops for the smaller contact size (Fig. 7(b)) than for the larger contact size (Fig. 7(a)). For the larger contact size, plastic flow mainly occurs parallel to the interface

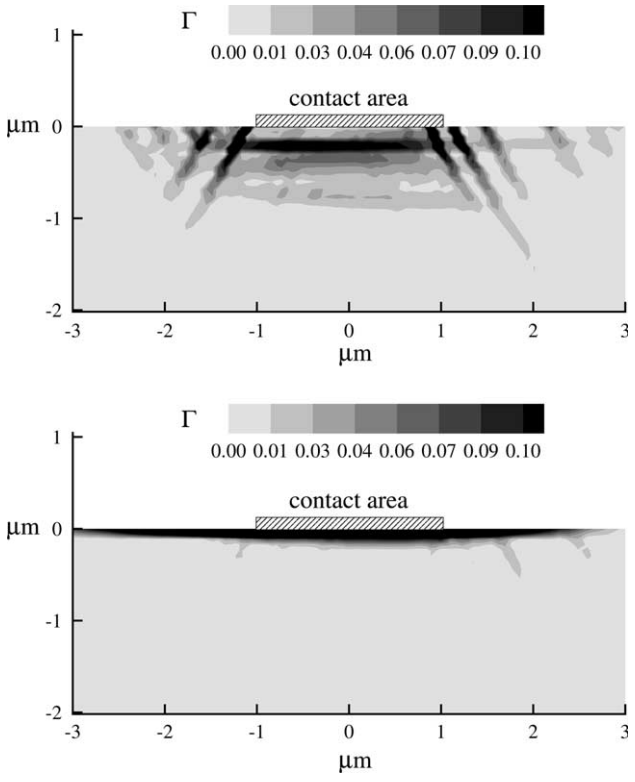

Fig. 11. Contours of the total slip Γ at $U = 0.05$ μm for the $a = 2$ μm contact. (a) The reference material with $\rho_{src} = 72/\mu m^2$ and (b) material with $\rho_{src} = 155/\mu m^2$. The contact surface is indicated in each case.

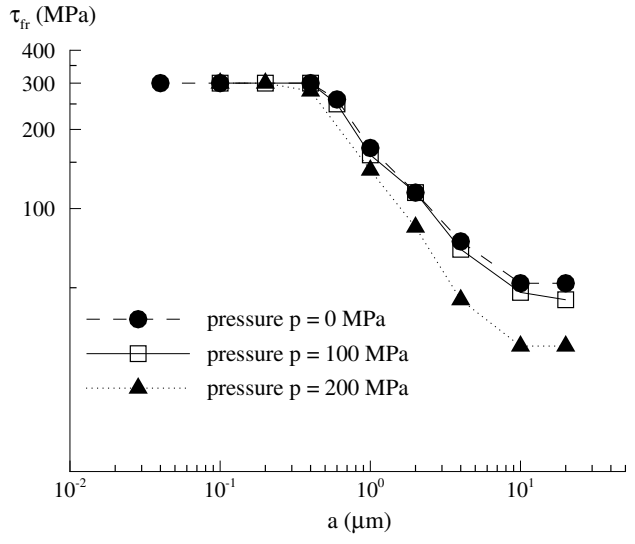

Fig. 12. Effect of normal pressure on the friction stress ($U_{fr} = 0.05$ μm). The calculations were carried out with reference material properties.

whereas there is more slip on the slip systems oblique to the interface for the smaller contact size. These dislocation structures pertain to the initiation of sliding. Once significant sliding, with the accompanying large plastic strains, has taken place other dislocation structures can emerge [2,3].

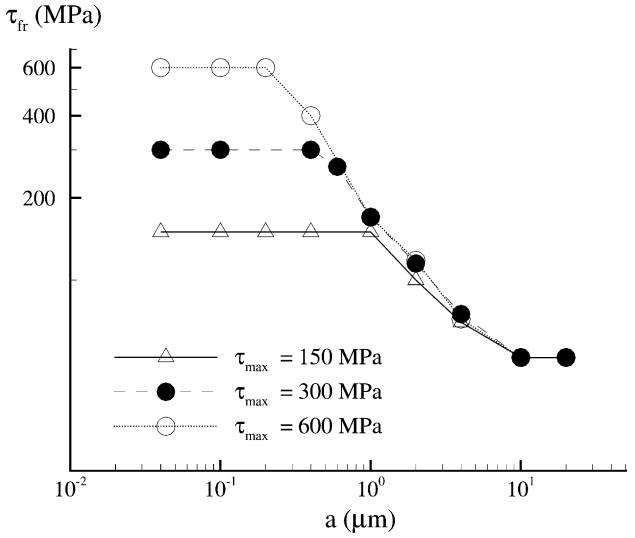

Fig. 13. Effect of the cohesive strength on the friction stress ($U_{fr} = 0.05$ μm). The calculations were carried out on the material with $\rho_{src} = 72/\mu m^2$.

5. Conclusions

We have carried out analyses of the initiation of sliding in single crystals under plane strain conditions. Plastic flow arises from the collective motion of discrete dislocations which nucleate from initially present internal Frank-Read sources. The adhesive properties are embedded in a cohesive surface constitutive relation. Two cohesive relations were used; in one the shear traction decays to zero with increasing sliding, while in the other the shear traction does not decrease from its maximum value.

- For sufficiently small contact sizes, adhesion dominates and the friction stress is equal to the cohesive strength, while for sufficiently large contacts plasticity dominates and the friction stress is approximately equal to the flow strength. For intermediate contact sizes, the friction stress is contact-size dependent.
- A very similar size dependence is found for the both the softening and the non-softening cohesive constitutive relations.
- For two of the dislocation source densities considered (20 and $72/\mu m^2$), the friction stress exhibits an inverse square root dependence on contact size in the transition regime between its small contact size upper-shelf value and its large contact size lower-shelf value. When the source density is sufficiently large ($155/\mu m^2$ in the calculations here), this scaling is lost.
- A normal pressure on the contact region less than or equal to twice the tensile yield strength has a negligible effect on the friction stress; the effect of a greater contact pressure (four times the tensile yield strength) is significant for larger contacts but remains negligible for sufficiently small contacts.

- The main effect of the cohesive strength is to set the small contact size upper-shelf value in the friction stress versus contact size relationship. The curve of friction stress versus contact size is nearly independent of cohesive strength once the friction stress falls below the cohesive strength.

Acknowledgements

Support from the General Motors Cooperative Research Laboratory at Brown University is gratefully acknowledged. We are pleased to acknowledge Prof. K.L. Johnson of Cambridge University and Prof. K.S. Kim of Brown University for insightful discussions during the course of this work.

References

[1] Bowder FP, Tabor D. The friction and lubrication of solids. Oxford: Clarendon Press; 2001.
[2] Kuhlmann-Wilsdorf D. In: Rigney DA, editor. Fundamentals of friction and wear of materials. USA: ASM; 1980.
[3] Rigney DA. Mater Res Innovat 1998;1:231.
[4] Green AP. Proc Roy Soc Lond A 1955;228:191.
[5] Tangena AG, Wijnhoven PJM. Wear 1985;103:345.
[6] Ohmae N. J Tribol ASME 1987;109:330.
[7] Chang RW, Etsion I, Bogy DB. J Tribol ASME 1987;109:257.
[8] Kapoor A, Johnson KL, Williams JA. Wear 1996;200:38.
[9] Storåkers B, Biwa S, Larsson P-L. Int J Solids Struct 1997;34:3061.
[10] Kogut L, Etsion I. J Tribol ASME 2004;126:34.
[11] Polonsky IA, Keer LM. J Tribol ASME 1996;118:335.
[12] Polonsky IA, Keer LM. Proc Roy Soc Lond 1996;452:2173.
[13] Homola HM, Israelachvlli JN, McGuiggan PM, Gee ML. Wear 1990;136:65.
[14] Carpick RW, Agrait N, Ogletree DF, Salmeron M. J Vac Sci Technol B 1996;14:1289.
[15] Carpick RW, Agrait N, Ogletree DF, Salmeron M. Langmuir 1996;12:505.
[16] Hurtado JA, Kim KS. Proc Roy Soc Lond A 1999;455:3363.
[17] Hurtado JA, Kim KS. Proc Roy Soc Lond A 1999;455:3385.
[18] Rice JR, Thompson R. Philos Mag 1973;29:73.
[19] Bhushan B, Nosonovsky M. Acta Mater 2003;51:4331.
[20] Landman U, Luedtke WD, Ringer EM. In: Singer IL, Pollock HM, editors. Fundamentals of friction: macroscopic and microscopic processes. Dordrecht: Kluwer; 1992.
[21] Gerde E, Marder M. Lett Nat 2001;413:285.
[22] Cleveringa HHM, Van der Giessen E, Needleman A. Int J Plasticity 1999;15:837.
[23] Deshpande VS, Needleman A, Van der Giessen E. Acta Mater 2002;50:831.
[24] Bradley RS. Philos Mag 1934;13:853.
[25] Johnson KL, Kendall K, Roberts AD. Proc Roy Soc Lond A 1971;324:301.
[26] Derjaguin BV, Muller VM, Toporov YP. J Colloid Interface Sci 1975;53:314.
[27] Magius D. J Colloid Interface Sci 1992;150:243.
[28] Johnson KL. Proc Roy Soc Lond A 1997;453:163.
[29] Kim KS, McMeeking RM, Johnson KL. J Mech Phys Solids 1998;46:243.
[30] Xu X-P, Needleman A. Model Simul Mater Sci Eng 1993;1:111.
[31] Van der Giessen E, Needleman A. Model Simul Mater Sci Eng 1995;3:689.
[32] Freund LB. Adv Appl Mech 1994;30:1.
[33] Cleveringa HHM, Van der Giessen E, Needleman A. J Mech Phys Solids 2000;48:1133.
[34] Kubin LP, Canova G, Condat M, Devincre B, Pontikis V, Bréchet Y. Solid State Phenom 1992;23–24:455.
[35] Cleveringa HHM, Van der Giessen E, Needleman A. Mater Sci Eng A 2001;317:37.
[36] Deshpande VS, Needleman A, Van der Giessen E. Acta Mater 2003;51:1.
[37] Johnson KL. Proc Instn Mech Engrs C 1999;214:11.
[38] Caroli C, Nozieres P. In: Persson BNJ, Tosatti E, editors. Physics of Sliding Friction: Proceedings of the NATO Advanced Research Workshop and Adriatico research conference, Turin, Italy; 1995.
[39] Beltz GE, Rice JR. Acta Mater 1992;40:S321.